



Periodic structures of Sn self-inserted between graphene interlayers as anodes for Li-ion battery



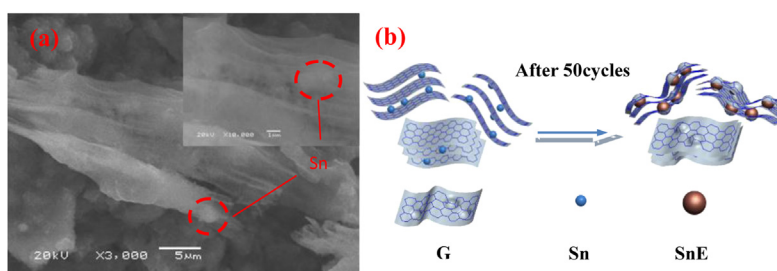
Xiangyang Zhou, Youlan Zou, Juan Yang*

School of Metallurgical and Environment, Central South University, Changsha 410083, China

HIGHLIGHTS

- Periodic structures of graphene/Sn/graphene composites were synthesized facilely.
- Graphene serves as both the reducing agent and supporting matrix.
- This structure prevents the contact of Sn/Sn particles and the overlap of G/G sheets.
- It improves cycle and rate performances of lithium ion battery using this anode.

GRAPHICAL ABSTRACT



ARTICLE INFO

Article history:

Received 27 September 2013

Received in revised form

4 December 2013

Accepted 7 December 2013

Available online 18 December 2013

Keywords:

Periodic structures

Tin

Graphene nanosheets

Lithium ion battery

ABSTRACT

A simple approach has been reported to prepare Sn nanoparticle/graphene nanosheets (G/Sn) as an anode material for lithium ion batteries. Sn nanoparticles with size of ~ 5 nm are directly grown and uniformly distributed between graphene interlayers. Graphene nanosheets act as the reducing agent and supporting matrix. Optimized G/Sn electrode with appropriate Sn content exhibits improved capacity (838.4 mAh g^{-1} at 0.1 A g^{-1} after 100 cycles) and cycling stability ($684.5, 639.7, 552.3$ and 359.7 mAh g^{-1} at $0.5, 1, 2$ and 5 A g^{-1} respectively after 100 cycles). The enhanced electrochemical performance should be related to the designed layer-by-layer (G/Sn/G) structure, the synergism between the elastomeric space and large area of graphene, and the excellent conductivity of the Sn nanoparticles.

© 2013 Elsevier B.V. All rights reserved.

1. Introduction

Developing anode materials with high capacity and cycling stability is one of the most hot researches in lithium ion battery (LIB) [1–3]. Sn or Sn-based anode materials have been considered as one of the most promising anode candidates for its relatively high conductivity and theoretical capacity (994 mAh g^{-1}) [4,5]. While drastic volume change of Sn occurs during charging/discharging process, which leads to cracking and pulverization of the

electrodes and eventually quick fading of capacity [6,7]. To address this problem, fabricating carbonaceous composite material such as Sn/C [6,8,9] anodes and Sn/CNTs [10–12] anodes seems to be an applicable strategy. But still, the performance of Sn-based anode is not very satisfactory, especially the huge fading of capacity after long-term cycling at high charge–discharge current density, resulting from disintegration of the whole electrode.

A novel carbonaceous material, graphene(G) with the maximum surface area of $2630 \text{ m}^2 \text{ g}^{-1}$ and high conductivity, is believed to be a type of potential buffering matrix for Sn-based electrodes [13–15]. Uniform insertion of metal Sn between graphene layers could alleviate the aggregation of metal Sn, segregate the overlap of graphene during synthesis process and confine the volume change of Sn during charging/discharging cycling. Many of the previous

* Corresponding author. Tel./fax: +86 0731 88836329.

E-mail addresses: lanlinliao@163.com (X. Zhou), 15874853145@139.com (Y. Zou), zytan0935@csu.edu.cn, hncsyjy308@163.com (J. Yang).

reports involved in the preparation of Sn contained graphene nanocomposites [16–20]. S.Q. Chen et al. [18] have reported that tin-graphene nanocomposite prepared by microwave hydrothermal method. S.Z. Liang et al. [19] have reported that tin nanoparticles coated with carbon were embedded in graphene and showed the capacity of 662 mAh g^{-1} at 0.1 A g^{-1} after 100 cycles, even 417 mAh g^{-1} at 1 A g^{-1} . However, most of the reported methods either have difficulties in high synthesis costs or complex synthesis processes, so far have been proved not to be very successful in improving the cyclability of Sn-based electrodes.

In this report, a simple and facile synthesis route is developed to prepare Sn/graphene composites via hydrothermal technique and subsequent calcination process. SnO_2 nanoparticles are in-situ generated between the graphite oxide layers, and the graphite oxide is simultaneously transformed into graphene nanosheets by hydrothermal process. Thus, Sn nanoparticles were anchored between the graphene nanosheets layer-by-layer rather than simply decorating on the surface of graphene after calcination process. In addition, silica nanoparticles serve as the template to confine the growth of tin and the overlap of the graphene, making sure that the final product reserves enough space and keeps the layer-by-layer insertion structure. This unique structure prevents the contact of Sn/Sn nanoparticles and the overlap of G/G nanosheets, further assures high electrode conductivity. Graphene nanosheets with certain elasticity could also alleviate the expansion of metal Sn, thus leading to an excellent electrochemical performance for lithium-ion batteries.

2. Experimental section

2.1. Synthesis of G/Sn composites

Graphite oxide was first synthesized by a modified Hummers' method [11]. In a typical synthesis, 140 mg graphite oxide was dispersed into 60 mL ethanol by ultrasonication for 2 h. The resultant GO dispersion was labeled as solution A. Solution B was prepared by dissolving 0.88 g $\text{SnCl}_4 \cdot 5\text{H}_2\text{O}$ and 5 mL colloidal silica sol ($\sim 20 \text{ nm}$) into 60 mL ethanol. Then, the two solutions were mixed, transferred to an airtight reactor and kept in an oven at 160°C for 2 h. After the autoclave cooled down, the product was processed with 20% HF for 4 h to exclude colloidal silica and washed several times with de-ionized water. Finally, the precipitate was dried under vacuum at 0°C for 2 days, followed by heating in a tube furnace under high-purity Ar at 1000°C for 2 h at a heating rate of $5^\circ\text{C} \cdot \text{min}^{-1}$. The as-prepared sample designated as G/Sn.

2.2. Characterizations

Scanning Electron Microscopy (SEM, JSM-6360LV, Japan) Brunauer–Emmett–Telle (BET, QUADRASORB SI, Quanta-chrome Instruments U.S/N₂) and transmission Electron Microscopy (TEM, JEM-2100F, Japan) images were taken to characterize the morphologies and structures of the sample. Atomic Force Microscopy (AFM) was conducted on NanoScope (R) III instrument operating in a tapping mode. The sample for AFM measurement was prepared by depositing a drop of much diluted G/Sn composite dispersion on mica substrate and drying at room environment. X-ray Diffraction (XRD) patterns were recorded on RigakuD/max-2550V X-ray diffractometer with Cu K α radiation. The Sn weight portion was calculated based on the thermogravimetric analysis (TGA, SDTQ600) data. Laser Raman Spectroscopy (OLYMPUS, BX41) with an excitation wave length of 488 nm by a KAr matrix was used to observe the type of graphene material.

2.3. Electrochemical tests

Electrochemical performances were performed with 2025 coin cells using Li foil as counter electrode. The working electrode was prepared by mixing 80% composite, 10% carbon black, and 10% polyvinylidene fluoride (PVDF) into *N*-methylpyrrolidinone (NMP). The slurry was pasted onto copper foil and dried overnight at 120°C in vacuum. The electrolyte was 1 mol L^{-1} LiPF_6 dissolved in a mixture of ethylene carbonate (EC)/diethyl carbonate (DMC) (1:1, by volume). The cells were assembled in an argon-filled glove box (1220/750, Shanghai). Galvanostatic discharge/charge experiments were performed over a potential range of 3 V–0.01 V vs. Li^+/Li using a battery tester (CT-2001A, Wuhan). Electrochemical workstation (Solartron 1470E, USA) was taken to measure the cyclic voltammograms (CV). CV experiment was performed in the range of 3 V–0.01 V vs. Li^+/Li at a scanning rate 0.1 mV s^{-1} . Here the total weight of the G/Sn sample was used to calculate the capacity values.

3. Results and discussion

The preparation process for G/Sn periodic structures consists of four main steps as illustrated in Fig. 1A. Typically, GO dispersion is obtained from graphite by using strong oxidation agents and ultrasonication. Tin oxide (SnO_2) and colloidal silica (SiO_2) nanoparticles are sandwiched between GO dispersion by a hydrothermal process, during which the interval between GO sheets increases. SiO_2 acts as dispersant to separate the SnO_2 nanoparticles, amplifies the distance of the neighboring two GO layers and prevents the overlap of GO nanosheets. Then, the colloidal silica is excluded from the obtained G/ SnO_2 / SiO_2 hybrids by 20% HF. Finally, the G/ SnO_2 is heated under Ar flow at 1000°C for carbothermal reduction.

X-ray diffraction (XRD) experiments were carried out to reveal the composition and structure changes of G, G/ SnO_2 , and G/Sn samples during the four steps. As shown in Fig. 1B, the symbol diffraction peak of GO around $2\theta = 11.4^\circ$ cannot be found but a very broad peak at $2\theta = 24^\circ$ is observed in G sample, indicating that most oxygen functional groups have been removed from the carbon framework. This is in consistent with the Fourier Transform Infrared (FTIR) results (Fig. S1, Supporting information). It should be emphasized that the diffraction peak at $2\theta = 24^\circ$ in graphene is rather broad and conspicuously distinct from graphite [18]. The highly broadened diffraction peaks in GO/ SnO_2 sample are indicative of the formation of SnO_2 nanocrystals with very small size. After heat treatment as shown in G/Sn sample, all intense peaks are well indexed to metal Sn (JCPDS No. 65-0296) and the sharpness of diffraction peaks indicates complete crystallinity of the tin phase. The crystallite size of G/Sn is estimated to be 5.9 nm according to the Debye–Scherrer formula. No SnO_2 crystalline phase is detected, implying that nearly all the SnO_2 nanoparticles have been reduced in contrast with the diffraction peaks of GO/ SnO_2 sample. No obvious peaks relative to graphene are observed in G/Sn samples, which might be attributed to the disordered stacking effect of graphene sheets in the composites. Raman spectroscopy is a useful tool to characterize the graphene material. The relative intensity ratio of $I(\text{D})$ and $I(\text{G})$ represents the degree of disorder in the graphene materials. Fig. 1C shows the Raman spectra of G, G/ SnO_2 , and G/Sn samples. Raman spectra of the G sample displays a strong G band at 1590 cm^{-1} , a D weak band at 1359.28 cm^{-1} . The value of $I(\text{D})/I(\text{G})$ for G is 0.81 (less than 1), indicating that G sample still kept the graphite structure except for a limited amounts of disordered structure. When the Sn amount was added and GO was hydrothermally reduced, the D peak intensity became prominent, and the intensity ratio of D and G for G/ SnO_2 is more than 1 (~ 1.01). This can be due to the defects introduced into the G/ SnO_2 sample

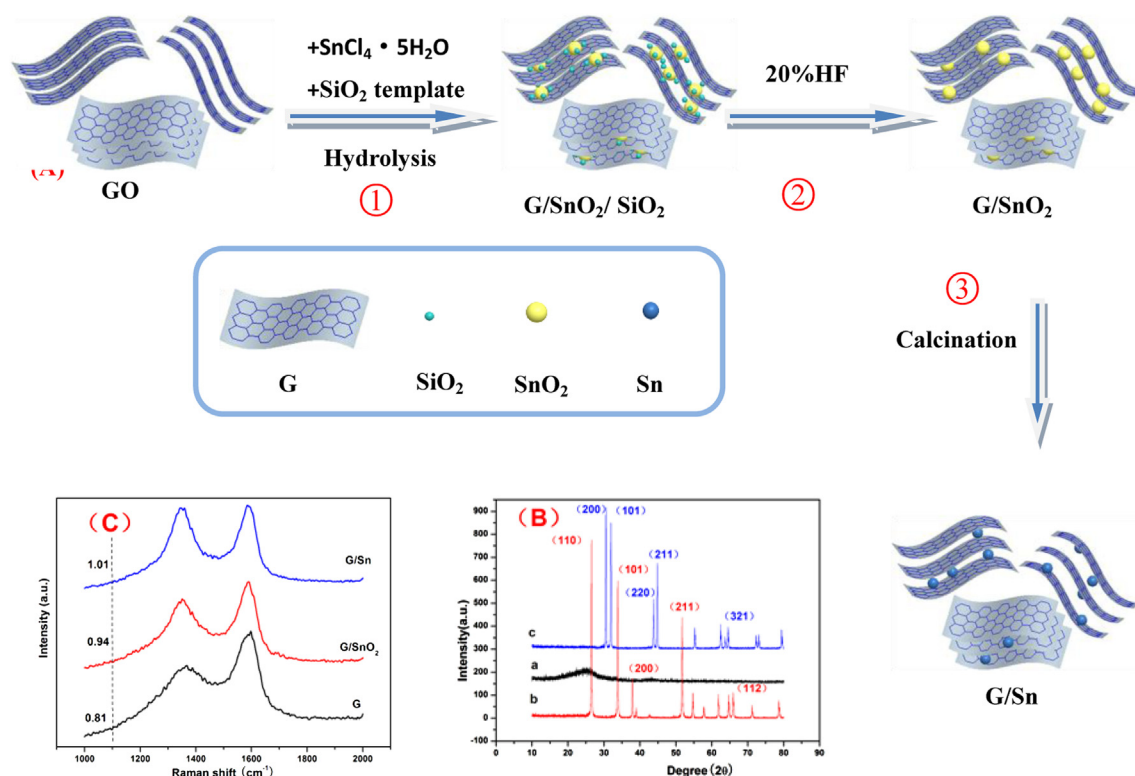


Fig. 1. A) Schematic of procedures for the synthesis of G/Sn sample; ① SnO_2 and SiO_2 nanoparticles were decorated on GO nanosheets via a hydrolysis process; ② SiO_2 was removed from G/ SnO_2 / SiO_2 sample; ③ G/ SnO_2 was transformed into G/Sn nanosheets through carbothermal reduction. B) XRD patterns of G (a); GO/ SnO_2 (b); G/Sn (c) samples; (C) Raman spectra of G; GO/ SnO_2 ; G/Sn samples.

during preparation. After thermal treatment, The value of $I(D)/I(G)$ for G/Sn sample is 0.94, suggesting that the quality of the G/Sn sample is better than that of the G/ SnO_2 sample [21,22].

Fig. 2a presents the typical SEM image of G sample, showing a stack of layered laminas composed of complex fold and void space. It is conspicuous to observe the edges of individual sheets, including the crumpled and continuous areas. Fig. 2b shows graphene sheets are loosely stacked into continuous films without apparent stacking order. No Sn particles are detected on the surface, implying that nearly all the Sn particles are sandwiched between graphene layers. TEM image (Fig. 3c) identifies that the Sn nanoparticles with an average particle size of ~ 5 nm are dispersed into the graphene layers. The uniform distribution of Sn nanoparticles among graphene is due to the in-situ carbothermal reduction between the graphene layers. The void space between the two graphene layers acts as an inclosed generator. Graphene served as reducing agent to generate Sn, and as barrier layer to prevent Sn crystal nucleus from growing up or contacting with neighbor Sn nucleus. AFM images (Fig. 3e and f) could also be used to detect the thickness of the graphene nanosheet and the G/Sn composite. Taping mode section analysis displays the height of G/Sn composite is about 8 nm (Fig. 3e) from macroscopic perspective. Fig. 3f shows defects on the surface of graphene for the transformation of C to CO and CO_2 under higher magnification. Thus, the height of the individual graphene nanosheet can be detected from the defect and the value between two arrows is about 1.5 nm [23]. It is noted that the thickness of the graphene sheet is much higher than the theoretical height. This is probably because there is a layer of absorbed ethanol molecules between the sample and the substrate. Considered that the height of graphene sheet (Fig. 3f) and the Sn particles are sandwiched between two graphene sheets, the height of Sn particles were about 5 nm. The tin amount in the G/Sn sample is

determined to be 60.6 wt% by thermogravimetric analysis (TGA) after the product had been calcined at 1000°C in air (where Sn was transformed into SnO_2 , and G was completely removed from the sample). Furthermore, just as other nanoparticles with huge specific surface area are beneficial to shorten Li-ion transportation path, so too are G/Sn composite. Compared with the study of B. Luo, in which the specific surface of G/Sn/G composites is reported $90.7\text{ m}^2\text{ g}^{-1}$ [16], the actual specific surface area of G/Sn composite ($153.22\text{ m}^2\text{ g}^{-1}$) is higher. The increased surface area is probably due to the less size of Sn nanoparticles (comparing with B. Luo). Sn nanoparticles could act as a spacer to prevent the restacking of graphene sheets.

Electrochemical performance of the G/Sn electrode is investigated in coin cells using Li foil as the counter electrode. The specific capacities given below are based on the total mass of the composite. Fig. 3a shows the cyclic voltammogram (CV) of the initial 3 cycles at a scan rate of 0.1 mV s^{-1} between 0.01 and 3 V. The reduction peak at around 1.05 V in the first scan may be due to the formation of the solid electrolyte interphase (SEI) films or the irreversible reduction of tiny SnO_2 on the surface of Sn [20]. The difference near this potential between the first and the following scans indicates a different initial lithiation route for the first cycle. Another three reduction peaks at 0.37, 0.5 and 0.62 V in the first cycle can be assigned to the multistep electrochemical reactions (lithiation) of Sn with lithium ions to form various Li_xSn_y , while four separated oxidation peaks at 0.46, 0.61, 0.72 and 0.8 V on the positive-current side correspond to the extraction of lithium ions from the formed Li_xSn_y alloy phases [24–26]. The unchanged peak current intensity, except the first cycle, implies the structure of synthesized electrode tends to be stable. Furthermore, a group of weakening peaks at 0–0.01 V demonstrate reversible reactions of lithium ions with graphene (Fig. S2).

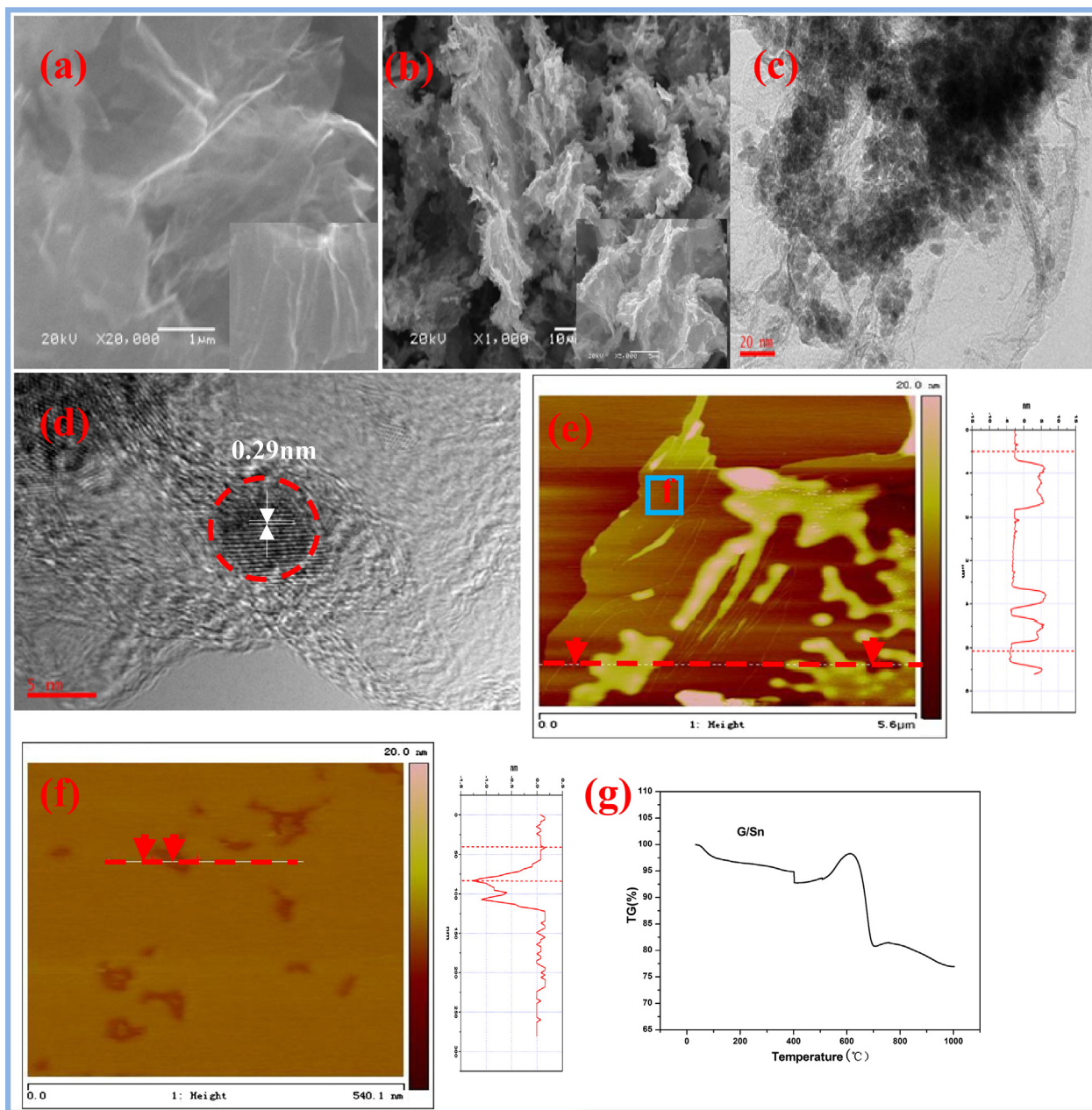


Fig. 2. SEM image of G (a), SEM (b) and TEM (c, d) images of G/Sn sample, and TGA curves of G/Sn sample, heating rate $10^{\circ}\text{C min}^{-1}$.

Fig. 3b shows the galvanostatic charge/discharge curves at a current density of 0.1 A g^{-1} and cycling performance plot of the G/Sn electrode at different current densities ($0.1, 0.5, 1, 2$ and 5 A g^{-1}) in comparison to those of graphene and G/SnO₂ electrodes with cutoff potential at 0.01 V and 3 V . The first discharge curve of G/Sn electrode presents a steep voltage drop to about 1 V and an incline down to the cutoff voltage of 0.4 V . No obvious long voltage plateau at about 1 V can be observed, indicating that metallic Sn was entirely encapsulated inside the graphene interlayers (not exposed to the electrolyte) [24]. The incline is followed by a long voltage plateau at about 0.4 V which is indicative of the typical voltage trend of Sn and associated with different stages of phase transition from Sn to Li_xSn_y [25–28]. At the positive going potential scan, the first charge curve of the G/Sn electrode undergoes two gradient intervals ($0.4\text{--}0.62\text{ V}$ and $0.62\text{ V--}0.8\text{ V}$), and a long voltage plateau at about 0.62 V , which is mainly related to the reversible lithium ion

extraction from Li_xSn_y [16–18,29]. Whereas, G and G/SnO₂ electrodes show unobvious voltage plateau at 0.4 V (during lithiation period) and 0.62 V (during delithiation period) at the first discharge/charge step. The initial discharge and charge capacities of the G electrode are 2208.4 and 1108 mAh g^{-1} , corresponding to a coulombic efficiency of 50.2% at a current density of 0.1 A g^{-1} . The high lithium storage capacity could be attributed to a large amount of boundary point or defects in graphene nanosheets. It should be noted that there is a considerable capacity loss for forming solid electrolyte interphase (SEI) films in the interface of graphene [30,31]. The G/SnO₂ and G/Sn electrodes delivered the discharge capacities of 1908.1 and 1839.4 mAh g^{-1} with the coulombic efficiencies of 60.5% and 77.7% , respectively. The high coulombic efficiency of G/Sn electrode could be ascribed to the contributions of the absence of SnO₂, which irreversibly consume large amount of Li-ions in the first cycle. The part of irreversible capacities loss for G/

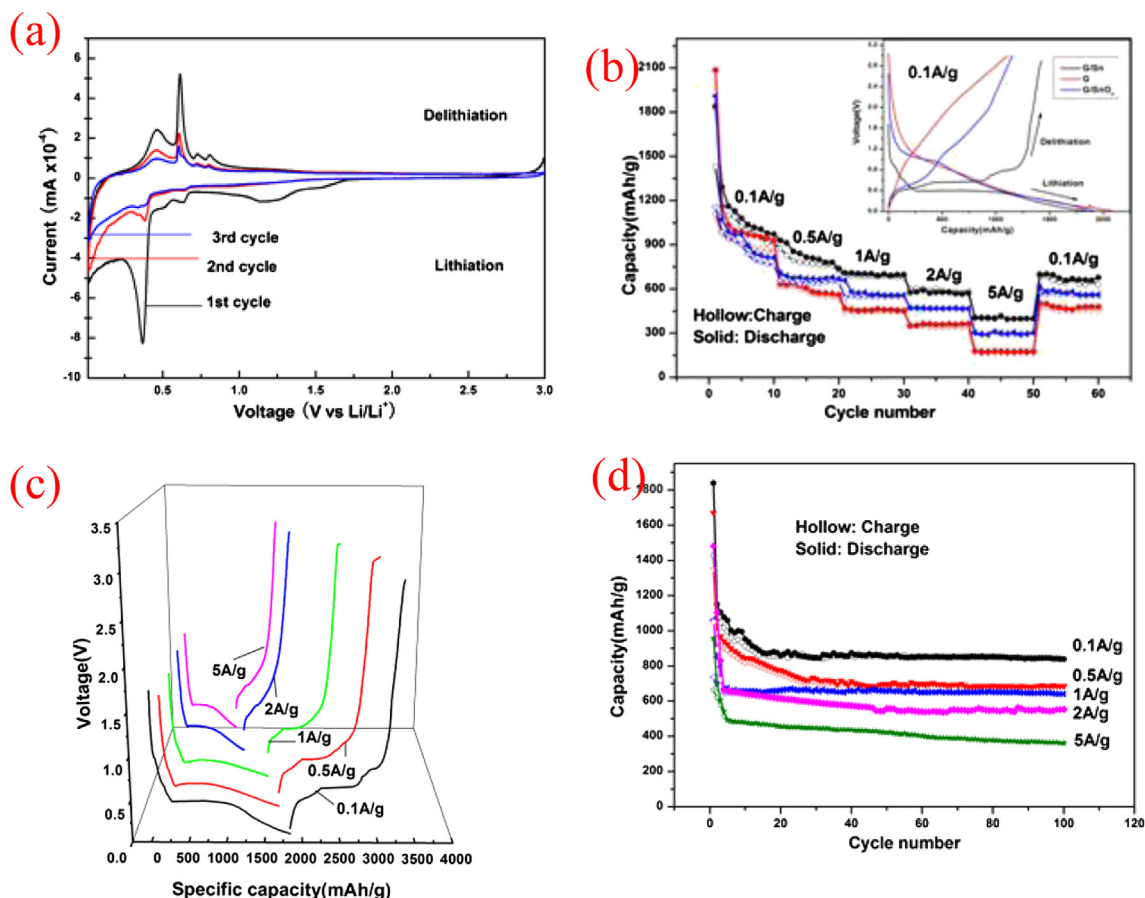


Fig. 3. (a) Cycle voltammograms of G/Sn electrode, the scan speed is 0.1 mV s^{-1} . (b) The discharge/charge and cycling performance plots of G, G/SnO₂, and G/Sn electrodes at current densities of 0.1, 0.5, 1, 2 and 5 A g^{-1} ; (c) the discharge/charge curves of G/Sn electrodes in the first cycle at stepwise current densities; (d) rate performances of G/Sn electrodes at different current densities.

Sn electrode could be caused by the formation of the SEI films on the surface of the electrodes and the volume expansion of Sn nanoparticles [18–20,32].

When tested for the cycling performance at different current densities, the G electrode shows a stable cycling performance at each appointed current densities, but with a relatively low first cycle discharge capacity of about 1108 mAh g^{-1} , which decreases to 478.9 mAh g^{-1} at stepwise cycle. Even though the first discharge capacity of the G/SnO₂ electrode is comparable with the value of G/Sn electrode, the transformation of SnO₂ consumes a large amount of Li-ion and damage the original structure of G/SnO₂, further cycling leads to a rapid capacity decay than G/Sn electrode after stepwise cycles. The comparison result shows that the G/Sn anode combines the merits of both graphene and Sn components and displays both large Li-storage capability and improved cycle performance. The capacity of the G/Sn electrode remains at around 911 mAh g^{-1} after the first ten cycles at a constant current of 0.1 A g^{-1} . Although the capacity decreases to about 721, 679.8, 576.4, and 398 mAh g^{-1} upon subsequent each ten cycling at a higher current of 0.5, 1, 2 and 5 A g^{-1} . These values are still close to the theoretical capacity of commercially used graphite anodes (e.g. 372 mAh g^{-1}). The capacity remains stable at about 628.4 mAh g^{-1} after returning to a constant current of 0.1 A g^{-1} for ten cycling. This result is superior to the prior reported results of Sn/graphene nanocomposites [24]. The introduction of graphene buffer layers would be benefit to limited the huge volume expansion/shrinkage during the continuous lithiation/delithiation reactions and protect

the structural integrity of the G/Sn electrodes, leading to the effective electrical contact, and rapid lithium ion transformation.

The voltage profiles of G/Sn electrode at different current densities in the first cycle can be seen in Fig. 3c. The electrode delivered first discharge/charge capacities of 1839.4/1429.6, 1671.7/1351.7, 1482.8/1051.6, 1060.9/736.6 and $954.8/663 \text{ mAh g}^{-1}$ at the current densities of 0.1, 0.5, 1, 2 and 5 A g^{-1} , respectively. The irreversible capacity may be caused by the formation of a solid electrolyte interphase and the lithium ions reaction with unreduced functional groups of the graphene. The shapes of voltage profiles are similar for five pairs of discharge/charge curves, which show the stability of the composite as an anode. After the first cycle, the G/Sn electrode showed highly reversible behavior. The G/Sn electrode maintained the charge capacity of 838.4, 684.5, 639.7, 552.3 and 359.7 mAh g^{-1} at each current density after 100 cycles (Fig. 3d).

Attempts have been made to compare the electrochemical performance of the G/Sn samples with different Sn amount (Fig. 4). TGA (Fig. 4a) calculates that the weight ratio of Sn in G/Sn1 and G/Sn2 samples are 60.6%, 66.1% and 71.9%, respectively. Fig. 4b shows the curves of specific capacity versus potential for the three different G/Sn samples at a constant current density of 0.1 A g^{-1} . The three G/Sn electrodes express nearly the consistent charge and discharge trend unless a more conspicuous slope at about 0.8 V emerged in G/Sn1 and G/Sn2 samples during the discharge process, indicating that more part of Sn nanoparticles expose to the outside surface of the graphene nanosheets and transform to SnO₂. The G/Sn1 and G/Sn2 electrodes deliver the first discharge/charge

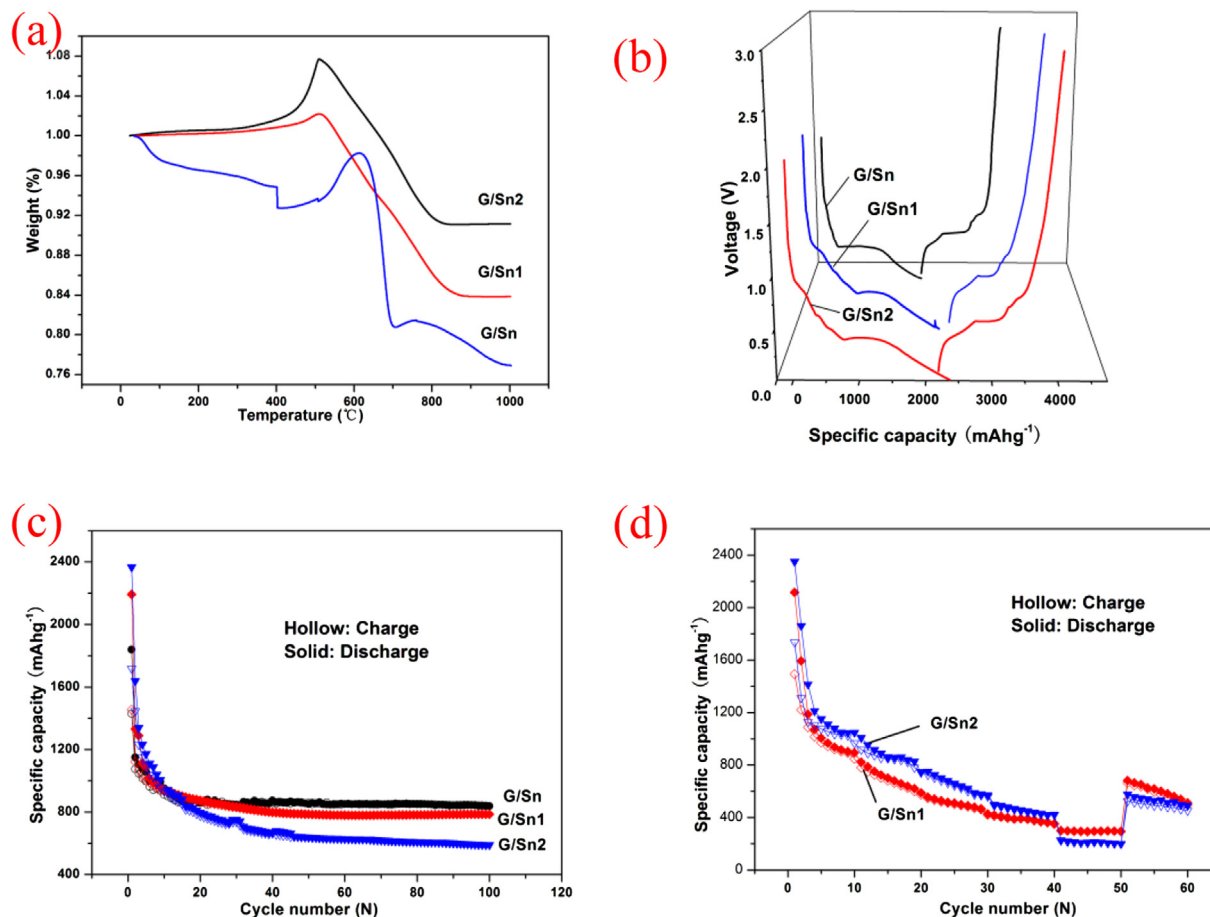


Fig. 4. (a) TGA curves of G/Sn, G/Sn1 and G/Sn2 samples, heating rate 10 °C min⁻¹; (b) The first discharge/charge and (c) cycling performance of G/Sn, G/Sn1 and G/Sn2 electrode at the current density of 0.1 A g⁻¹; (d) rate performances of G/Sn, G/Sn1 and G/Sn2 electrodes at current densities of 0.1, 0.5, 1, 2 and 5 A g⁻¹.

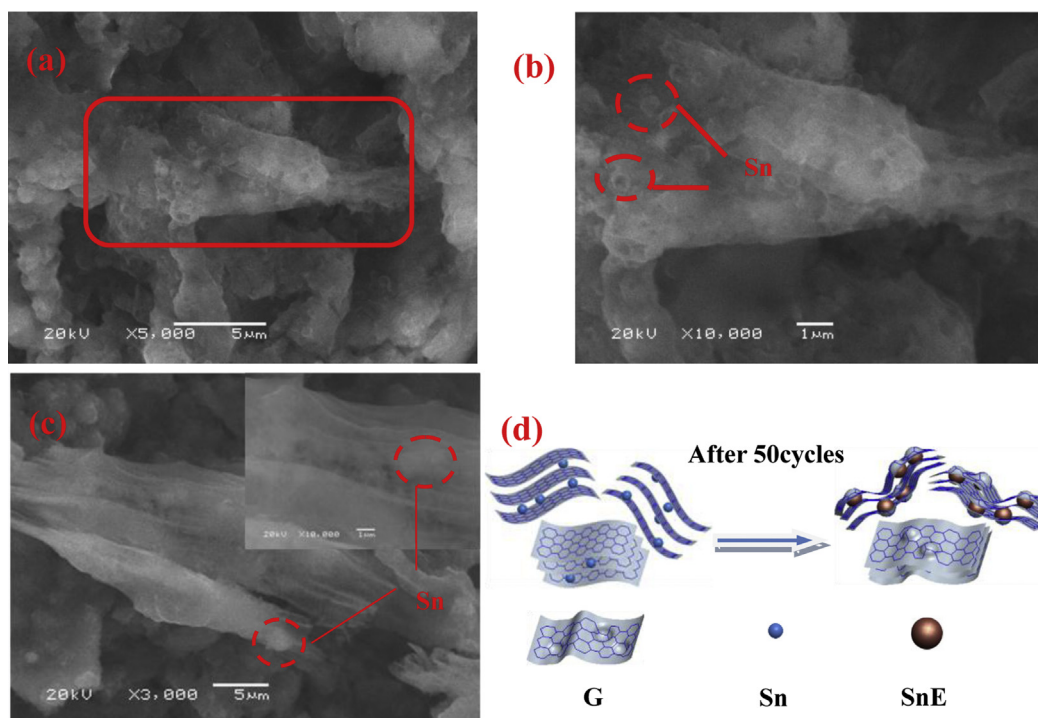


Fig. 5. (a–c) SEM images of G/Sn sample after 50 cycles at 0.1 A g⁻¹; (d) schematic illustration of the volume effect of the G/Sn sample after 50 cycles.

capacities of 2191.6/1454.5 and 2365.9/1718.2 mAh g⁻¹, with the coulombic efficiency of 66.36% and 72.6% respectively. These higher first specific capacities than G/Sn electrode could be attribute to the contribution of Sn amount and the synergistic effect of the periodic structure. However, the lower coulombic efficiency than G/Sn electrode should be ascribed to the exposed of Sn nanoparticles and the formation of SEI layers on the surface of the electrodes. After 100 cycles, the three electrodes (G/Sn, G/Sn1 and G/Sn2) maintain the charge capacity of 838.4, 786.2 and 589 mAh g⁻¹, according to Fig. 4c. It is noted that the higher Sn amount leads to a more drastic capacity fading for the G/Sn1 and G/Sn2 electrodes. With the increase of Sn amount, more part of the Sn nanoparticles expose to the outside surface of the graphene nanosheets, and the interval of the neighboring Sn particles get closer. Large volume changes of Sn nanoparticles during the charge/discharge process with lithium impel the contact and agglomeration of the neighboring Sn particles, even profoundly destroy the inclosed generator (from TEM Fig. 3c) and the integrity of the electrode [18]. Fig. 4d demonstrates the cycling performance of the two electrodes at different current densities (0.1, 0.5, 1, 2 and 5 A g⁻¹). It should be noted that the capacity decreases with the increase of the current densities, and the capacity abruptly rises again after the current density return to 0.1 A g⁻¹. This indicates that the G/Sn1 and G/Sn2 electrodes are likely suitable to high power electrical applications. However, the increase of the Sn amount (from 60.6% to 71.9%) leads to the higher capacity loss, indicating that the electrode with higher Sn amount is no beneficial for the cycling performance of the electrode.

The morphology of the G/Sn electrode after 50 cycles at 0.1 A g⁻¹ have been studied as shown in Fig. 5a–c. SEM image shows the graphene material retains its original lamina structure. The hexagonal carbon network and elasticity property of graphene facilitate to limit the volume expansion/contraction and the aggregation of Sn nanoparticles. Metallic Sn nanoparticles were entrapped by graphene nanosheet with particle size growing up to about 500 nm. It is observed that the repeated lithium alloying/dealloying processes have not leaded to pulverized Sn particle, and the Li–Sn alloy was formed or decomposed in-situ area, avoiding aggregation with the neighboring Sn atoms or the neighboring graphene sheets. However, the graphene layers were drastically humped due to the huge expansion of Sn (SnE) simulated as Fig. 4d. It prevents the structure from collapse during the subsequent cycles.

4. Conclusions

A simple and practical synthesis route is developed to prepare Sn/graphene composites using a hydrothermal-assistant carbothermal reduction process. The emphasis to this method is the in-situ synthesis of Sn nanoparticles and graphene nanosheets, which segregate the overlap of graphene and prevent the contact of Sn nanoparticles. This material exhibits an improved capacity rate capability and cycling stability. The preparation of G/Sn periodic structures is very meaningful both for fundamental study of Sn-based composites and for industrial application.

Acknowledgments

This work is financially supported by Nature Science Foundation of China. (NO: 51204209, 51274240).

Appendix A. Supplementary data

Supplementary data related to this article can be found at <http://dx.doi.org/10.1016/j.jpowsour.2013.12.034>.

References

- [1] S. Chu, A. Majumdar, *Nature* 488 (2012) 294–303.
- [2] M. Armand, J.M. Tarascon, *Nature* 451 (2008) 652–657.
- [3] J.B. Goodenough, Y. Kim, *Chem. Mater.* 22 (2010) 587–603.
- [4] G. Ferrara, C. Arbizzani, L. Damen, M. Guidotti, M. Lazzari, F.G. Vergottini, R. Inguanta, S. Piazza, C. Sunseri, M. Mastragostino, *J. Power Sources* 211 (2012) 103–107.
- [5] L.P. Xu, C.J. Kim, A.K. Shukla, A. Dong, T.M. Mattox, D.J. Milliron, J. Cabana, *Nano Lett.* 13 (2013) 1800–1805.
- [6] W.S. Chang, C.M. Park, H.J. Sohn, *J. Electroanal. Chem.* 671 (2012) 67–72.
- [7] J. Hassoun, G. Derrien, S. Panero, S. Scrosati, *Adv. Mater.* 19 (2007) 2336–2340.
- [8] W.M. Zhang, J.S. Hu, Y.G. Guo, S.F. Zheng, L.S. Zhong, W.G. Song, L.J. Wan, *Adv. Mater.* 20 (2008) 1160–1165.
- [9] Y.H. Xu, Q. Liu, Y.J. Zhu, Y.H. Liu, A. Langrock, M.R. Zachariah, C.S. Wang, *Nano Lett.* 13 (2013) 470–474.
- [10] Y. Wang, M.H. Wu, Z. Jiao, J.Y. Lee, *Chem. Mater.* 21 (2009) 3210–3215.
- [11] L. Noerochim, J.Z. Wang, S.L. Chou, D. Wexler, H.K. Liu, *Carbon* 50 (2012) 1289–1297.
- [12] N. Tombros, L. Buit, I. Arfaoui, T. Tsoufis, D. Gournis, P.N. Trikalitis, S.J. Molen, P. Rudolf, B.J. Wees, *Nano Lett.* 8 (2008) 3060–3064.
- [13] W.S. Hummers, R.E. Offeman, *J. Am. Chem. Soc.* 80 (1958), 1339.
- [14] E.J. Yoo, J. Kim, E. Hosono, H.S. Zhou, T. Kudo, I. Honma, *Nano Lett.* 8 (2008) 2277–2282.
- [15] B.J. Kim, H. Jang, S.K. Lee, B.H. Hong, J.H. Ahn, J.H. Cho, *Nano Lett.* 10 (2010) 3464–3466.
- [16] B. Luo, B. Wang, X.L. Li, Y.Y. Jia, M.H. Liang, L.J. Zhi, *Adv. Mater.* 24 (2012) 3538–3543.
- [17] B. Luo, B. Wang, X.L. Li, Y.Y. Jia, M.H. Liang, L.J. Zhi, *Adv. Mater.* 24 (2012) 1405–1409.
- [18] S.Q. Chen, Y. Wang, H. Ahn, G.X. Wang, *J. Power Sources* 216 (2012) 22–27.
- [19] S.Z. Liang, X.F. Zhu, P.C. Lian, W.S. Yang, H.H. Wang, *J. Solid State Chem.* 184 (2011) 1400–1404.
- [20] Z. Qin, Z.J. Li, M. Zhang, B.C. Yang, R.A. Outlaw, *J. Power Sources* 217 (2012) 303–308.
- [21] S.H. Kim, Y. Yu, Y.Z. Li, T. Xu, J.F. Zhi, *J. Mater. Chem.* 22 (2012) 18306–18313.
- [22] Z.J. Fan, W. Kai, J. Yan, T. Wei, L.J. Zhi, J. Feng, Y.M. Ren, L.P. Song, F. Wei, *ACS Nano* 5 (2011) 191–198.
- [23] K.H. Liu, L. Liu, Y.F. Luo, D.M. Jia, *J. Mater. Chem.* 22 (2012) 20342–20352.
- [24] L.W. Ji, Z.K. Tan, T. Kuykendall, E.J. An, Y.B. Fu, V. Battaglia, Y.G. Zhang, *Energ. Environ. Sci.* 4 (2011) 3611–3616.
- [25] M. Marcinek, L.J. Hardwick, T.J. Richardson, X. Song, R.J. Kostecki, *J. Power Sources* 173 (2007) 965–971.
- [26] M. Sathish, S. Mitani, T. Tomai, A. Unemoto, I. Honma, *J. Solid State Electrochem.* 16 (2012) 1767–1774.
- [27] G.X. Wang, B. Wang, X.L. Wang, J. Park, S.X. Dou, H. Ahn, K.J. Kim, *Mater. Chem.* 19 (2009) 8378–8384.
- [28] J.S. Zhu, D.L. Wang, L. Wang, X.S. Lang, X.L. You, *Electrochim. Acta* 91 (2013) 323–329.
- [29] D. Deng, J.Y. Lee, *Angew. Chem. Int. Ed.* 48 (2009) 1660–1663.
- [30] C.H.H. Lucas, A.J.L. Peinado, J.D.L. Gonzalez, M.J.R. Cervantes, R.M.M. Aranda, *Carbon* 33 (1995) 1585–1592.
- [31] H.K. Jeong, Y.P. Lee, R.J. Lahaye, M.H. Park, K.H. An, I.J. Kim, C.W. Yang, C.Y. Park, R.S. Ruoff, Y.H. Lee, *J. Am. Chem. Soc.* 130 (2008) 1362–1366.
- [32] Y.Q. Zou, Y. Wang, *ACS Nano* 5 (2011) 8108–8114.